Bioinspired *Two-in-One* Nanotransistor Sensor for the Simultaneous Measurements of Electrical and Mechanical Cellular Responses

Hongyan Gao,[1] Feiyu Yang,[2] Kianoosh Sattari,[3] Xian Du,[2,4] Tianda Fu,[1] Shuai Fu,[1]
Xiaomeng Liu,[1] Jian Lin,[3] Yubing Sun,[2,4,5] Jun Yao*[1,4,5]

---

[1]Department of Electrical and Computer Engineering, University of Massachusetts, Amherst, 01003, USA.

[2]Department of Mechanical and Industrial Engineering, University of Massachusetts, Amherst, 01003, USA.

[3]Department of Mechanical and Aerospace Engineering, University of Missouri, Columbia, Missouri 65211, USA.

[4]Institute for Applied Life Sciences, University of Massachusetts, Amherst, 01003, USA.

[5]Department of Biomedical Engineering, University of Massachusetts, Amherst, 01003, USA.

* Corresponding author. E-mail: juny@umass.edu (J.Y.)

ABSTRACT:

The excitation-contraction dynamics in cardiac tissue are the most important physiological parameters for assessing developmental state. We demonstrate integrated nanoelectronic sensors capable of simultaneously probing electrical and mechanical cellular responses. The sensor is configured from a 3D nanotransistor with its conduction channel protruding out of the plane. The structure promotes not only a tight seal with the cell for detecting action potential *via* field effect but also a close mechanical coupling for detecting cellular force *via* piezoresistive effect. Arrays of nanotransistors are integrated to realize label-free, sub-millisecond, and scalable interrogation of correlated cell dynamics, showing advantages in tracking and differentiating cell states in drug studies. The sensor can further decode vector information in cellular motion beyond typical scalar information acquired at the tissue level, hence offering an improved tool for cell mechanics studies. The sensor enables not only improved bioelectronic detections but also reduced invasiveness through the two-in-one converging integration.

Summary: 3D transistors assembled from suspended Si nanowires work as cell probes to detect correlated electrophysiological and mechanical activities.

Introduction

Electrical and mechanical responses from cells are important state indicators in human-derived cardiac tissues (*1*), which are promising models for cardiac disease study, drug test and regenerative medicine (*2, 3*). Importantly, since these two activities are intricately correlated through the excitation-contraction (EC) coupling, the simultaneous measurement of them is highly desirable and critical for identifying physiological and pathological mechanisms (*4, 5*). For example, the weakening of the EC coupling in cells, which can lead to arrhythmias (*6*), may be best revealed by the tracking of both electrical and mechanical cellular activities. Despite the importance, it remains challenging to simultaneously measure the two processes (*4, 5, 7-9*). Traditional optical methods relied on fluorescence labeling to indicate bioelectrical signals and morphological tracing to detect biomechanical behaviors (*5, 7-9*). The two methods were combined to study EC dynamics in individual cells, revealing information otherwise missed from single-parameter measurement (*9*). However, they are limited in the scalable tracking of fast kinetics in 3D tissue due to reduced temporal resolution and accessibility (*5, 10, 11*); and molecular labeling may also compromise cell contractility or induce toxicity (*9*).

Electrical sensors can enable label-free, multi-channel interrogation at high temporal resolution (*11,12*). They can be further integrated on flexible and porous scaffolds to innervate the tissue (*13-18*), retrieving deep-tissue information that is less accessible by other techniques. Nevertheless, current electrical sensors such as microelectrode and transistor arrays are limited to probing single property of electrical or mechanical response only (*11-18*). Efforts have been made recently to combine one sensor with a complementary one for the simultaneous measurement (*5, 7, 19-21*), although the heterogeneity leads to considerable challenges in synchronization or scalability. For example, nanopatterned microelectrode was fabricated on an atomic force microscope (AFM) tip for force-electrogram recording in a cell (*19*), which was limited in scalability and accessibility with the single cantilever in an AFM setup. Microelectrodes and pairs of interdigitated electrodes were also combined for synchronized recordings of electrical and mechanical activities in cardiac tissue (*20, 21*). However, the pair of interdigitated electrodes for motion tracking through impedance measurement took a large size (*20, 21*), limiting the measurement to single- or few-device scale with a low resolution at the tissue level.

Overall, the strategy of combining two types of sensors inevitably leads to heterogeneity in integration and/or signal acquisition, which furthers limit the scalability and spatial resolution (*i.e.*, increased space occupation with two sensors). The latter introduces not only challenge in achieving cell-resolution recording, but also a spatial difference in acquired signals to limit the accuracy when studying correlated dynamics. In addition, it also increases the invasiveness to biological tissue. In contrast to the monofunctionality in developed electrical sensors (*11-18*), biological organelles often merge multiple sensory mechanisms for efficient parallel signaling (*22*). For example, neurites sense not only action potential (AP) but also mechanical stimuli for developmental guidance (*23*).

Results

Basic device structure and characterizations

We draw inspiration from the multifunctional biofilaments and propose a 3D nanotransistor constructed from a nanowire to converge sensing functions. The proposed device has a convex structure by translating a semiconducting silicon (Si) nanowire across a microscale bar or microbar (Fig. 1A). The source and drain contacts on the substrate and the microbar supporting the apex of nanowire form a triangular configuration to confer structural stability. The geometric freedom in the suspended nanowire allows for the translation of cellular force into mechanical deformation or strain change in the nanowire (Figs. 1B, C), which can be electrically detected through the piezoresistive effect (*24, 25*). Meanwhile, the nanotransistor can also detect AP (Fig. 1C) through the field effect (*11-14*). As biomechanical and bioelectrical processes can fall into different frequency domains (*8, 12*), both can be electrically detected and differentiated in a single device.

Some unique advantages can be inferred. First, the suspended nanowire geometry resembles biofilaments in an extracellular matrix (*26*), to which cells attach. Therefore, the sensor geometry may facilitate cell attachment for signal transductions. Second, Si nanowire has a giant piezoresistive effect (*24*), offering enhanced force sensitivity down to tens of pN (*25*). This is crucial for resolving cellular forces at nN or sub-nN level (*8*). Note that Si nanowire has a strength for sustaining μN force (*27*), providing mechanical robustness against cellular force. Third, the 3D protruding feature can tighten the cell-device seal to improve the detection of electrical activities (*12*).

The nanotransistor arrays were constructed using a scalable nanowire 3D assembly (*25*) based on a 'combing' technique (figs. S1, S2) (*28, 29*). Electrical contacts were defined and passivated by standard microfabrication (fig. S1). A matrix of 8 × 8 nanotransistors were integrated in an area of ~0.8 × 0.8 mm^2 (Fig. 1D). The device features a single nanowire with its two segments suspended symmetrically across the microbar (~1.4 μm high), spanning an average distance of 7.8 ± 0.9 μm (Figs. 1E, F). With a nanowire diameter ~30-50 nm, the nanotransistor occupies a projected area < 0.4 μm^2, much smaller than typical microelectrodes or strain sensors used in tissue recording (*15-18, 30-34*). A device yield ~63-93% was achieved (figs. S1, S2). Compensated by the small device size, high-density integration achieving cellular or subcellular resolution is feasible.

Electrical characterizations were performed in the devices to reveal the potential for recording electrical and mechanical cellular responses. The as-assembled nanowire is estimated to experience a maximal strain <0.3%, which is in the elastic region and far below the fracture limit (*27*). As a result, the sensitivity to field potential (4.2 ± 1.0 μS/V), characterized by water-gate response (Fig. 1G), was unaffected and close to that in unstrained Si-nanowire transistors capable of detecting AP (*14, 35, 36*). The collective sensing performance is comparable to different transistors used for cellular detection (table S1) (*36-42*). The temporal response in the nanotransistor was measured to be faster than 0.3 ms in solution environment (fig. S3), which was consistent with previous study and capable of resolving electrophysiological responses (*43*). Meanwhile, mechanical testing and simulation revealed an average gauge factor of 7.6 ± 1.0 × 10^2 in the nanowires (Fig. 1H; fig. S4), consistent with the giant piezoresistive effect observed previously (*24*). The gauge factor is much larger than typical values in other piezoresistive sensors used for biomechanical detection in tissue (table S2) (*30-34*). The enhanced piezoresistive sensitivity in the Si nanowire thus constitutes a unique advantage in improving force resolution for cellular detection. Specifically, the estimated force resolution of ~33 pN in the device (fig. S4) was commensurate with the strength of protein bonds in cell adhesion (*44*) and much smaller than typical contractile forces (*e.g.*, 1-100 nN) revealed by micropost arrays (*8*), indicating the capability to track minute cellular force. The devices showed good uniformity in responding to both compressive (Fig. 1H) and tensile strain (fig. S5) for integrated signal analysis.

Cellular interfacing and recording

Above structural and functional properties have indicated the potential in the nanotransistor for multifunctional cellular probing. Human embryonic stem cell-derived cardiomyocytes (hESC-CMs), which are considered promising *in vitro* models of cardiac health and disease (*2, 3*), were cultured on the device substrate. The integrated nanotransistor arrays showed excellent biocompatibility (fig. S6), consistent with previous studies showing that the materials used in the device (*e.g.*, SU-8, Si) are biocompatible (*14, 45*). Imaging revealed that the cardiomyocytes formed close interface with the 3D device structures without breaking the suspended nanowires (fig. S7). These results facilitated the device arrays to successfully record signals from the monolayer cardiomyocytes forming synchronized contraction (movie S1). Recordings from eight representative devices showed synchronized periodic signals (Fig. 2A). The signal frequency (~ 0.4 Hz) was consistent with typical contractile frequency in hESC-CMs (*2*). In each signal period, the broad peak was preceded by a sharp spike (Figs. 2B, C). The broad peak and sharp spike had average (*N*=25) signal-noise ratios larger than 7 and 4, respectively, confirming the sensing validity (*35*). Both signals were different from possible artifact induced during testing (fig. S4B). Analysis of the sharp spikes shows uniform potential waveforms with an average duration ~20 ms and converted amplitude of ~1.5 mV (Fig. 2D), characteristic of extracellular AP from hESC-CMs (*2*). Recordings from human induced pluripotent stem cell-derived cardiomyocytes (hiPSC-CMs) showed similar results (fig. S8). The nanotransistor arrays also enabled real-time mapping of signal propagation across the tissue (fig. S9), revealing a conduction velocity ~ 4.5 cm/s consistent with values in *in vitro* hESC-CMs (*3*).

The broad peaks were revealed to originate from mechanical contraction. First, the peak featured a slow rising edge (~600 ms) (Fig. 2C), which was distinct from the fast initiation of an intercellular AP (*3*). In fact, this signal was exclusively observed in the 3D nanotransistors here but not in previous electrical cellular sensors (*14-17*). Second, the average duration of the signals ($\Delta t_1 \sim 1.2 \pm 0.4$ s, Fig. 2E) was consistent with the contractile time span in hESC-CMs. In particular, the evolution of the signal shape closely matched that of the contractile force (*46*). Third, concurrent Ca^{2+} imaging revealed that the evolution of Ca^{2+} transient, which is released from the sarcoplasmic reticulum to activate contraction in cardiomyocytes (*47*), closely matched that of the broad peak (fig. S10). These analyses have confirmed the origin of broad peaks from cellular mechanical response. As a result, the time delay between the AP and initiation of the mechanical signal ($\Delta t_2 \sim 35 \pm 10$ ms, Fig. 2F) characterizes the latency time of AP-triggered Ca^{2+} release from the sarcoplasmic reticulum. The value revealed from electrical recording was consistent with value from optical measurement (*48*). The integrated nanotransistor arrays offer the advantage for scalable measurement. The high temporal resolution enabled the differentiation of temporal dynamics among individual batches of cell cultures (fig. S11).

Implementing devices in drug tests

We performed drug tests to further reveal the potential of implementing the sensors in pharmacological and pathological studies in cells. Blebbistatin, an inhibitor of myosin essential for motile machinery, was used to suppress cell contraction (Fig. 3A). The electrical recordings showed a substantial decrease in the amplitude of the mechanical signals after adding blebbistatin (20 μM), whereas the amplitude of AP maintained the similar level (Figs. 3B, C). The maintenance of AP indicated unaffected electrophysiological activity in cells, revealing that the signal depression was exclusively related to suppression of cell contraction. Washing out blebbistatin restored the mechanical signals (fig. S12). Notably, the evolution in signal amplitude (Fig. 3C) matched the decay profile of sarcomere shortening in cardiomyocytes perfused with blebbistatin (*49*), showing that the sensor can closely track drug effect in developmental stages.

Conversely, lidocaine, a Na^+ channel blocker, was added to suppress Na^+ influx which contributes mostly to extracellular AP (Fig. 3D). The electrical recording (Fig. 3E) showed a prominent suppression in AP but no obvious effect on the mechanical signal after the introduction of lidocaine (20 μM). The sensor revealed further details of the AP evolution, in which the amplitude reduced from ~ 10 nS to ~ 2 nS and the duration increased from ~19 ms to ~40 ms (Fig. 3F). This trend was consistently observed in different cells (fig. S13). The observed trends were consistent with the drug mechanism in both reducing and slowing Na^+ influx (*50*).

A Ca^{2+} dysfunctional model was also built by treating the cardiomyocytes with isradipine, a Ca^{2+} channel blocker used for treating a wide variety of cardiovascular disorders (Fig. 3G, inset). The treatment of isradipine (20 nM) led to the apparent suppression of mechanical signal in ca. 100 s (Figs. 3G, H), which was consistent with the mechanism of Ca^{2+}-activated contraction (*47*). Unlike the effect from blebbistatin, the sensor revealed a concurrent decrease in AP (Figs. 3H, I), consistent with the mechanism of a concurrent suppression of Na^+-channel current by isradipine (*51*). Washing out isradipine restored both signals (fig. S14), showing the robustness in the sensor for tracking correlated E-C dynamics across different stages. The isradipine effect (Fig. 3I) can be readily differentiated from blebbistatin (Fig. 3C) and lidocaine (Fig. 3F) effects by the sensor with the E-C dynamics tracked simultaneously.

Additional drug test by the treatment of E-4031, a K^+ channel blocker, yielded fluctuations in contractile frequency and amplitude captured by the sensor (fig. S15), consistent with traits in K^+ blocker-induced arrhythmia behavior. The treatment of norepinephrine, on the other hand, yielded increased contractile frequency and an alteration of the conduction pathway captured by the sensors (fig. S16).

These drug tests have shown that the 3D nanotransistor can capture the details of electrical and mechanical activities throughout different cell stages. The correlated information offers unique advantage in differentiating cell states and drug effects, which otherwise may not be achieved through single-parameter measurement of mechanical or electrical response. As a result, it offers a promising candidate to assemble sensing platforms for cell-mechanism studies and drug models.

Electrical recording and analysis of mechanical responses

Electrical recording of mechanical properties in cardiac tissue offers additional advantages for constructing organs-on-chips (*30-34*). Previous piezoresistive sensors often employed a thin-film form factor that was fully coupled to a supporting substrate, which can compromise the force transduction. The device sizes or force resolutions were not adequate to resolve cellular mechanical responses (table S2) (*30-34*), and the detection was largely limited to tissue resolution. By contrast, the 3D nanotransistor features a device size smaller than cell, a geometry decoupled from the substrate, and an enhanced force sensitivity, which are advantageous for detecting mechanical responses at cellular resolution.

We therefore further investigated the recordings of mechanical signals. The sensors detected both positive and negative signals (Fig. 2A), with the majority (~73%) being negative (fig. S17). This may be generally understood from the expectation that the cell-device interface may have influenced the translation of strain in the nanotransistor to be in the tensile or compressive region to yield different sensing signs. To better understand the results, simulations were performed to study the mechanical coupling between cell and device (Fig. 4A, fig. S18). As the device was much smaller than the cell, it was assumed to experience uniform local motion dominated by an in-plane component (*5*) characterized by an angle θ with respect to the nanowire axis (Fig. 4B, inset). The simulations show that the net strain in the nanowire transits from compressive to tensile when θ increases from 0° to 90° (Fig. 4B; fig. S18), with the average threshold angle ~25°. Consider a random distribution, ~72% of the devices are expected to experience tensile strain or a negative sensing signal, consistent with the experimental observation (fig. S17). Specifically, the strain distribution yields expected average values of 2.2×10^{-5} and -1.1×10^{-5} for tensile and compressive strain, respectively (Fig. 4B). Note that the average gauge factor of $7.6 \pm 1.0 \times 10^{2}$ revealed in the compressive strain region (fig. S4) can be used for tensile strain analysis as well, since the piezoresistive effect in Si nanowires was revealed to be linear within small strain region (*e.g.*, $\pm 10^{-4}$) (*24*). As a result, these strain values correspond to expected average conductance changes of -1.66% and 0.82%, respectively. These values are also close to experimental values of -1.67% and 0.48%, respectively (fig. S17).

The strain level (*e.g.*, $<10^{-4}$, Fig. 4B) experienced in the nanowire indicates that only a small displacement is induced at the cell-nanowire interface. Mechanical simulation reveals that the average displacement in the nanowire is no more than 10 nm (fig. S19A). This is consistent with expectation that cell adhering to a rigid plane is subject to a general boundary condition, in which the local contractile motion decreases with increasing proximity to the fixed plane (*52*). The nanotransistor thus is expected to experience much smaller local cellular motion than global one (*e.g.*, top cellular motion), due to its limited vertical height (~1.4 μm). Optical imaging revealed global cell motion but unobservable displacement in the suspended nanowires (fig. S19B; movie S2), further confirming above analysis. These results ensure that the cell and nanowire form a stable interface (*e.g.*, no sliding) during the dynamic contractile process for robust signal recordings. The high mechanical sensitivity in the nanotransistor ensures that the small displacement can still be well detected. Therefore, the nanotransistors can reliably capture the details of mechanical responses as shown below.

The correlation between the sensing signal and mechanical activity was investigated by combining the electrical recording with optical imaging. Cellular motion was revealed by analyzing consecutive image frames captured during a contractile cycle (Fig. 4C, fig. S20). A clear trend from contraction (II-IV) to relaxation (IV-VI) was shown. Specifically, the average displacement ($\overline{D}$) of cellular motion at the device region (middle panel, Fig. 4D) was computed and compared with the electrical recording (top panel), showing a close match between their evolutions. In particular, the slight asymmetry in the contractile dynamics featuring a slower relaxation was clearly captured in the electrical recording (*e.g.*, $t_{\text{rising}} : t_{\text{falling}} = 0.6 : 1.0$ s). Meanwhile, the local vectors of cellular motion in each frame were also analyzed (arrows in Fig. 4C). The average angle ($\overline{\theta}$) of the vectors with respect to the nanowire axis was above 75° throughout the contractile cycle (bottom panel, Fig. 4D). The $\overline{\theta}$, above the threshold value of 25° from simulation (Fig. 4B), was expected to induce a net tensile strain in the nanowire or a conductance decrease, which was consistent with the electrical recording (top panel, Fig. 4D). Analyses in cell contraction (Fig. 4E) producing positive sensing signal (top panel, Fig. 4F) showed consistently close match between the signal amplitude and cellular displacement (middle panel, Fig. 4F). However, the average $\overline{\theta}$ was below the threshold value of 25° (bottom panel, Fig. 4F), consistent with the expected compressive strain or a conductance increase.

Analyses from all sampled devices (N=15) showed consistent result that the electrical signals reliably tracked the cell contractile dynamics (fig. S21A, B). The correlation between the signs in electrical sensing signals and cell-nanowire interfacing angle $\overline{\theta}$ was consistent with simulation (fig. S21C). The consistence enabled the feasibility to establish a predictive model, in which the local cellular force may be quantified from the electrical recording signal assisted by a one-time optical registration of $\overline{\theta}$ (fig. S22). The analysis revealed a force range ~3-160 nN based on recorded electrical signals, which was consistent with reported range in human-derived cardiomyocytes (*53*). Note that the Si nanowire can readily resolve this force range due to its high force sensitivity (*e.g.*, < 0.1 nN) and robust mechanical strength (*e.g.*, >μN) (*27*). These results show that the 3D nanotransistor can differentiate and quantify cellular responses to provide additional information for cell studies, which was not possible with previous planar sensors. Multiple nanotransistors of different orientations may be combined to refine information from the contractile vector, transcending a mere amplitude (*i.e.*, scalar) detection in previous electrical platforms (*30-34*). In particular, since the nanotransistor is much smaller than the cell, a 'pixel' containing multiple devices can still achieve or approach cellular resolution. As the alignment of contraction can be an important indicator of maturation and disease states in cardiac tissue (*54, 55*), integrated nanotransistors may be used for the scalable monitoring of mechanical responses including vector information important for tissue modeling.

Discussion

In conclusion, we have demonstrated 3D nanotransistors capable of simultaneously probing both mechanical and electrical cellular responses. The simultaneous recordings enable the detailed tracking of cellular dynamics involving multiple biological processes at high spatiotemporal resolution, which are important for discerning cell states. The convergence of both functionalities in one device also helps to achieve 'equivalent scaling' to minimize invasiveness to tissue models. Other than the potential of implementing in planar biochips, the nanotransistors can also be integrated on mesh electronic scaffolds (*14-17*) to innervate *in vitro* models or deliver to living systems (*18*) for deep-tissue studies. Recent study has shown that both electrical AP signals and mechanical responses can be used to reveal gene expression in cardiac tissue (*56, 57*). Implementing the nanotransistor with correlated signal measurements may reveal broader phenotype-to-genotype correlation. As a result, the 3D nanotransistor, in its own or by combining data analytics, can provide new potential for cell/tissue-mechanism studies.

Materials and Methods.

Si Nanowire synthesis. Si nanowires were grown by a vapor–liquid–solid (CVD) method described previously (*25, 28*). Briefly, a Si substrate (Nova Electronic Materials) was cleaned by oxygen plasma (80 W, 1 min), immersed in a 0.1% (w/v) poly-L-lysine solution (Ted Pella) for 5 min, rinsed thoroughly with deionized water, and then immersed in the Au-nanoparticle solution (Ted Pella) for 5 min. The substrate with assembled Au nanoparticles was placed in a home-built CVD system for nanowire growth. The growth was carried out at 450 °C at a constant pressure of 30 torr with 2.5 standard cubic centimeters per minute (sccm) SiH_4 (99.9999%; Voltaix), 3 sccm B_2H_6 (100 ppm in H_2; Voltaix) and 10 sccm Ar (99.999%; Matheson) as reactant, dopant and carrier gases, respectively. The growth time was 60 min, producing an average length of ~40 μm.

3D Si nanowire assembly and device fabrication. The 3D Si nanowire structures were assembled following method developed previously (*25*). Detailed procedures are described in fig. S1. An alternative strategy is shown in fig. S2, which was mainly used for fabricating devices for *in vitro* studies. Assembled nanowire structures were defined with electrical contacts (Cr/Pd, 3/70 nm) using standard photolithography, metal evaporation, and lift-off processes. Briefly, LOR 5A (Kayaku Advanced Materials, Inc.) was spin-coated at 1000 rpm for 1 min followed by prebaking at 180°C for 5 min. Photoresist S1805 (Kayaku Advanced Materials, Inc.) was spin-coated at 1000 rpm for 1 min and prebaked at 115°C. Photolithography and electron-beam evaporation were used to define and deposit the metal source/drain contacts and interconnected (Cr/Pd, 3/70 nm). The contacts and interconnects were further passivated with a Si_3N_4 layer (~90 nm) to prevent current leakage in solution.

Cell culture. Cardiomyocytes were differentiated from human embryonic stem cells (hESCs, WAe009-A, H9) and human induced pluripotent stem cells (hiPSCs, generated from human primary T cells using episomal reprogramming) following methods described previously (*15, 58*). Briefly, both cell types were maintained in the 60 mm tissue culture dishes coated with 10 ug/mL Matrigel in DMEM-F12 (Gibco^{TM}) using Essential 8 medium (Gibco^{TM}) and sub-passaged every 3-4 days. During differentiation, cells were seeded in a 12-well plate for 2-3 days until confluency, then replaced with RPMI 1640 medium (Gibco^{TM}) plus 1% B27-insulin (Gibco^{TM}) and 8 μM CHIR99021 (Tocris Bioscience™) (day 0). After 24 h (day 1), the medium was changed to RPMI 1640 plus 1% B27-insulin. On day 3, day 5, and day 7, the medium was changed to RPMI 1640 plus 1% B27-insulin and 10 μM IWR-1-endo (Cayman Chemical), RPMI 1640 plus 1% B27-insulin, and RPMI 1640 plus 1% B27, respectively. The medium was then replaced with RPMI 1640 plus 1% B27 every other day. The contraction of cells was usually observed on day 8. During days 10-15, cardiomyocytes were ready for experiments. The cells were rinsed with 1 × DPBS to remove calcium and inhibit contraction, then incubated with 0.5 mL of 0.5 mM Trypsin-EDTA (Gibco^{TM}) for 5 mins in a 37°C incubator to dissociate into single cells. The EDTA was then aspirated, and the cells were dissociated by gently pipetting with 2 mL RPMI 1640 plus 1% B27 using a 1 ml pipet tip. The cells were transferred to a 15 mL conical tube and centrifuged at 250 g for 3 minutes, then resuspended with 2 mL RPMI 1640 plus 1% B27 supplemented with 10% Fetal Bovine Serum (Gibco^{TM}) and 10 µM Y-27632 ROCK inhibitor (Tocris Bioscience™). The device substrate integrated with nanotransistors was sterilized by incubating in 70% ethanol solution (1 h) at room temperature and then UV-treated (1 h). The device was coated with 20 µg/mL Matrigel in RPMI 1640 for 1 h at 37°C. Cells were seeded on the device substrate at the density of 3-5 × 10^5/cm^2. The cardiomyocytes were maintained using RPMI 1640 plus 1% B27 by changing the medium daily. Electrical recordings were typically performed starting from day 5 after the cell seeding.

Biocompatibility analysis. The biocompatibility analysis of the 3D Si nanowire device (fig. S6) was tested using the Live/Dead Assay Kit (Invitrogen^{TM}). Cardiomyocytes were cultured on the device for five days and then stained with green fluorescent calcein-AM (2 µM) and red fluorescent ethidium homodimer-1 (4 µM). Hoechst 33342 (Invitrogen^{TM}) was used to stain the nucleus of cardiomyocytes (blue fluorescent). The sample was incubated for 30 min at 37°C and 5% CO_2 and imaged (Leica, DMi8). The viability quantification was calculated by using the following equation (*17*):

$$Viability\% = \frac{Total\ cells\ (blue) - Dead\ Cell\ (red)}{Total\ cells\ (blue)} \times 100\%$$

Electrical measurements. The basic electrical characterizations in the nanotransistors were performed by using a semiconductor analyzer (Keysight B1500A). All *in vitro* electrical recordings were carried out at the ambient environment with an Au reference electrode. The conductance of the Si nanotransistors was measured with a DC bias set to 100 mV. The drain current was amplified with 12-channel home-built amplifier system (fig. S23) and the output data were collected at an acquisition rate of 30 kHz using a 16-channel A/D converter (Digidata 1440A; Molecular Devices) interfaced with a computer running pClamp 10.7 electrophysiology software (Molecular Devices, Axon Laboratory).

Imaging and analysis. The SEM images were acquired by a JSM-7001F system. Bright-field optical videos of cell motion at 18 frame per second (FPS) were acquired through a Zeiss Axio Examiner microscope system, equipped with a CCD camera (AxioCam 702 Mono Camera) and Zen Blue software. The resolution of each frame was 1960 × 1080 pixels covering an imaging area of ~980 × 540 µm^2. Details of imaging processing for cell-motion analysis are described in fig. S20.

Cell-device interface imaging. Following previous procedure (*59*), the cardiomyocytes were first fixed on the substrate with 4 % Paraformaldehyde (Electron Microscopy Sciences) for 20 min and then dehydrated by treatments of ethanol of successively increasing concentrations (30, 50, 70, 90%, 100%, 100%, 100%). After the dehydration, the cardiomyocytes were treated with a critical point drying process (Samdri-PVT-3D, Tousimis) for 10-15 min. Finally, a 5 nm Pd was sputtered on the sample to increase the conductivity for SEM imaging (fig. S7).

Calcium imaging. The living cardiomyocytes on the device substrate were rinsed with 1 mL Hepes Buffered Tyrode's Solution (Thermo Scientific™), and stained with Fluo-8AM (5 µM, AAT Bioquest). The cells were then incubated at 37°C for 1 hour. The device was then rinsed with Tyrode's solution for three times. The calcium transient signal (fig. S10) was recorded with Zeiss Axio Examiner microscope system equipped with a CCD camera (AxioCam 702 Mono Camera) and Zen Blue software at 12 FPS. The recorded signal was analyzed by ImageJ.

Simulations. Detailed simulation information of device mechanical response and cell-device interface can be found in fig. S4 and fig. S18, respectively.

References

1. D. M. Bers, Cardiac excitation-contraction coupling. *Nature* **415**, 198-205 (2002).
2. M. Clements, N. Thomas, High-throughput multi-parameter profiling of electrophysiological drug effects in human embryonic stem cell derived cardiomyocytes using multi-electrode arrays. *Toxicol. Sci*. **140**, 445-461 (2014).
3. D. Zhang, I. Y. Shadrin, J. Lam, H.-Q. Xian, H. R. Snodgrass, N. Bursac, Tissue-engineered cardiac patch for advanced functional maturation of human ESC-derived cardiomyocytes. *Biomaterials* **34**, 5813-5820 (2013).
4. J. I. Goldhabar, K. D. Philipson, Cardiac sodium-calcium exchange and efficient excitation-contraction coupling: implications for heart disease. *Adv. Exp. Med. Biol*. **961**, 355-364 (2013).
5. B. J. van Meer, L. G. J. Tertoolen, C. L. Mummery, Concise review: measuring physiological responses of human pluripotent stem cell derived cardiomyocytes to drugs and disease. *Stem Cells* **34**, 2008-2015 (2016).
6. N. Chopra, T. Yang, P. Asghari, E. D. Moore, S. Huke, B. Akin, R. A. Cattolica, C. F. Perez, T. Hlaing, B. E. Knollmann-Ritschel, Ablation of triadin causes loss of cardiac Ca^{2+} release units, impaired excitation–contraction coupling, and cardiac arrhythmias. *Proc. Natl. Acad. Sci.* **106**, 7636-7641 (2009).
7. J. D. Kijlstra, D. Hu, N. Mittal, E. Kausel, P. van der Meer, A. Garakani, I. J. Domian, Integrated analysis of contractile kinetics, force generation, and electrical activity in single human stem cell-derived cardiomyocytes. *Stem Cell Rep.* **5**, 1226-1238 (2015).
8. M. Unal, Y. Alapan, H. Jia, A. G. Varga, K. Angelino, M. Aslan, I. Sayin, C. Han, Y. Jiang, Z. Zhang, Micro and nano-scale technologies for cell mechanics. *Nanobiomedicine* **1**, 5 (2014).
9. T. J. Herron, P. Lee, J. Jalife, Optical imaging of voltage and calcium in cardiac cells & tissues. *Circ. Res.* **110**, 609-623 (2012).
10. F. S. Alfonso, T. Zhou, E. Liu, A. F. McGuire, Y. Yang, H. Kantarci, D. Li, E. Copenhaver, J. B. Zuchero, H. Muller, B. Cui, Lable-free optical detection of bioelectric potentials using electrochromic thin films. *Proc. Natl. Acad. Sci. USA* **117**, 17260-17268 (2020).
11. X. Dai, W. Zhou, T. Gao, J. Liu, C. M. Lieber, Three-dimensional mapping and regulation of action potential propagation in nanoelectronics-innervated tissues. *Nat. Nanotechnol*. **11**, 776-782 (2016).
12. M. E. Spira, A. Hai, Multi-electrode array technologies for neuroscience and cardiology. *Nat. Nanotechnol*. **8**, 83-94 (2013).
13. A. Zhang, C. M. Lieber, Nano-Bioelectronics. *Chem. Rev*. **116**, 215-257 (2015).
14. B. Tian, J. Liu, T. Dvir, L. Jin, J. H. Tsui, Q. Qing, Z. Suo, R. Langer, D. S. Kohane, C. M. Lieber, Macroporous nanowire nanoelectronic scaffolds for synthetic tissues. *Nat. Mater*. **11**, 986-994 (2012).
15. Q. Li, K. Nan, P. Le Floch, Z. Lin, H. Sheng, T. S. Blum, J. Liu, Cyborg organoids: implantation of nanoelectronics via organogenesis for tissue-wide electrophysiology. *Nano Lett.* **19**, 5781–5789 (2019).

16. J. Liu, T.-M. Fu, Z. Cheng, G. Hong, T. Zhou, L. Jin, M. Duvvuri, Z. Jiang, P. Kruskal, C. Xie, Z. Suo, Y. Fang, C. M. Lieber, Syringe-injectable electronics. *Nat. Nanotechnol.* **10**, 629-636 (2015).
17. A. Kalmykov, C. Huang, J. Bliley, D. Shiwarski, J. Tashman, A. Abdullah, K. Rastogi Sahil, S. Shukla, E. Mataev, W. Feinberg Adam, K. J. Hsia, T. Cohen-Karni, Organ-on-e-chip: Three-dimensional self-rolled biosensor array for electrical interrogations of human electrogenic spheroids. *Sci. Adv.* **5**, eaax0729 (2019).
18. G. Hong, C. M. Lieber, Novel electrode technologies for neural recordings. *Nat. Rev. Neurosci.* **20**, 330-345 (2019).
19. B. Desbiolles, M. M. Hannebelle, E. de Coulon, A. Bertsch, S. Rohr, G. Fantner, P. Renaud, Volcano-shaped scanning probe microscopy probe for combined force-electrogram recordings from excitable cells. *Nano Lett.* **20**, 4520-4529 (2020).
20. X. Zhang, L. Guo, H. Zeng, S. L. White, M. Furniss, B. Balasubramanian, E. Lis, A. Lagrutta, F. Sannajust, L. L. Zhao, B. Xi, X. Wang, M. Davis, Y. A. Abassi, Multi-parametric assessment of cardiomyocyte excitation-contraction coupling using impedance and field potential recording: A tool for cardiac safety assessment. *J. Pharmacol. Toxicol. Methods* **81**, 201-216 (2016).
21. F. Qian, C. Huang, Y.-D. Lin, A. N. Ivanovskaya, T. J. O'Hara, R. H. Booth, C. J. Creek, H. A. Enright, D. A. Soscia, A. M. Belle, R. Liao, F. C. Lightstone, K. S. Kulp, E. K. Wheeler, Simultaneous electrical recording of cardiac electrophysiology and contraction on chip. *Lab on a Chip* **17**, 1732-1739 (2017).
22. M. J. Berridge, The endoplasmic reticulum: a multifunctional signaling organelle. *Cell Calcium* **32**, 235-249 (2002).
23. D. E. Koser, A. J. Thompson, S. K. Foster, A. Dwivedy, E. K. Pillai, G. K. Sheridan, H. Svoboda, M. Viana, L. d. F. Costa, J. Guck, C. E. Holt, K. Franze, Mechanosensing is critical for axon growth in the developing brain. *Nat. Neurosci.* **19**, 1592-1598 (2016).
24. R. He, P. Yang, Giant piezoresistance effect in silicon nanowires. *Nat. Nanotechnol*. **1**, 42-46 (2006).
25. H. Gao, B. Yin, S. Wu, X. Liu, T. Fu, C. Zhang, J. Lin, J. Yao, Deterministic assembly of three-dimensional suspended nanowire structures. *Nano Lett.* **19**, 5647-5652 (2019).
26. J. K. Mouw, G. Ou, V. M. Weaver, Extracellular matrix assembly: a multiscale deconstruction. *Nat. Rev. Mol. Cell Biol*. **15**, 771-785 (2014).
27. Y. Zhu, F. Xu, Q. Qin, W. Y. Fung, W. Lu, Mechanical properties of vapor-liquid-solid synthesized silicon nanowires. *Nano Lett*. **9**, 3934–3939 (2009).
28. J. Yao, Y. Yan, C. M. Lieber, A nanoscale combing technique for the large-scale assembly of highly aligned nanowires. *Nat. Nanotechnol*. **8**, 329-335 (2013).
29. J. Yao, H. Yan, S. Das, J. F. Klemic, J. C. Ellenbogen, C. M. Lieber, Nanowire nanocomputer as a finite-state machine. *Proc. Natl. Acad. Sci. USA* **111**, 1259-1264 (2014).
30. T. A. Busbee, A. D. Valentine, F. S. Pasqualini, H. Yuan, M. Yadid, S.-J. Park, A. Kotikian, A. P. Nesmith, P. H. Campbell, J. J. Vlassak, J. A. Lewis, K. K. Parker, Instrumented cardiac microphysiological devices via multimaterial three-dimensional printing. *Nat. Mater*. **16**, 303-308 (2017).
31. J. U. Lind, M. Yadid, I. Perkins, B. B. O'Connor, F. Eweje, C. O. Chantre, M. A. Hemphill, H. Yuan, P. H. Campbell, J. J. Vlassak, K. K. Parker, Cardiac

microphysiological devices with flexible thin-film sensors for higher-throughput drug screening. *Lab Chip* **17**, 3692-3703 (2017).

32. K. Matsudaira, T.-V. Nguyen, K. H. Shoji, T. Tsukagoshi, T. Takahata, I. Shimoyama, MEMS piezoresistive cantilever for the direct measurement of cardiomyocyte contractile force. *J. Micromech. Microeng.* **27**, 105005 (2017).
33. D.-S. Kim, Y. W. Choi, A. Shanmugasundaram, Y.-J. Jeong, J. Park, N.-E. Oyunbaatar, E.-S. Kim, M. Choi, D.-W. Lee, Highly durable crack sensor integrated with silicone rubber cantilever for measuring cardiac contractility. *Nat. Commun*. **11**, 1-13 (2020)
34. H. Zhao, Y. Kim, H. Wang, X. Ning, C. Xu, J. Suh, M. Han, J. Pagan-Diaz Gelson, W. Lu, H. Li, W. Bai, O. Aydin, Y. Park, J. Wang, Y. Yao, Y. He, M. T. A. Saif, Y. Huang, R. Bashir, J. A. Rogers, Compliant 3D frameworks instrumented with strain sensors for characterization of millimeter scale engineered tissue. *Proc. Natl. Acad. Sci. USA* **118**, e2100077118 (2021).
35. T. Cohen-Karni, B. P. Timko, L. E. Weiss, C. M. Lieber. Flexible electrical recording from cells using nanowire transistor arrays. *Proc. Natl. Acad. Sci.* **106**, 7309-7313 (2009).
36. T. Cohen-Karni, Q. Qing, Q. Li, Y. Fang, C. M. Lieber. Graphene and nanowire transistors for cellular interfaces and electrical recording. *Nano Lett.* **10**, 1098-1102 (2010).
37. J. F. Eschermann, R. Stockmann, M. Hueske, X. T. Vu, S. Ingebrandt, A. Offenhäusser, Action potentials of HL-1 cells recorded with silicon nanowire transistors. *Appl. Phys. Lett.* **95**, 083703 (2009).
38. A. B. Calia, E. Masvidal-Codina, T. M. Smith, N. Schafer, D. Rathore, E. Rodriguez-Lucas, X. Illa, J. M. Dela Cruz, E. D. Corro, E. Prats-Alfonso, D. Viana, J. Bousquet, C. Hebert, J. Martinez-Aguilar, J. R. Sperling, M. Drummond, A. Halder, D. Dodd, K. Barr, S. Savage, J. Fornell, J. Sort, C. Guger, R. Villa, K. Kostarelos, R. C. Wykes, A. Guimera-Brunet, J. A. Garrido, Full-bandwidth electrophysiology of seizures and epileptiform activity enabled by flexible graphene microtransistor depth neural probes. *Nat. Nanotechnol*. **17**, 301–309 (2022).
39. B. M. Blaschke, M. Lottner, S. Drieschner, A. B. Calia, K. Stoiber, L. Rousseau, G. Lissourges, J. A. Garrido, Flexible graphene transistors for recording cell action potentials. *2D Mater*. **3**, 025007 (2016).
40. Y. Liang, M. Ernst, M, F. Brings, D. Kireev, V. Maybeck, A. Offenhäusser, D. Mayer, High performance flexible organic electrochemical transistors for monitoring cardiac action potential. *Adv. Healthcare Mater*. **7**, 1800304 (2018).
41. Y. Liang, F. Brings, V. Maybeck, S. Ingebrandt, B. Wolfrum, A. Pich, A. Offenhäusser, D. Mayer, Tuning channel architecture of interdigitated organic electrochemical transistors for recording the action potentials of electrogenic cells. *Adv. Funct. Mater.* **29**, 1902085 (2019).
42. A. Kyndiah, F. Leonardi, C. Tarantino, T. Cramer, R. Millan-Solsona, E. Garreta, N. Montserrat, M. Mas-Torrent, G. Gomila, Bioelectronic recordings of cardiomyocytes with accumulation mode electrolyte gated organic field effect transistors. *Biosens. Bioelectron.* **150**, 111844 (2020).
43. X. Duan, R. Gao, P. Xie, T. Cohen-Karni, Q. Qing, H. S. Choe, B. Tian, X. Jiang, C. M. Lieber, Intracellular recordings of action potentials by an extracellular nanoscale field-effect transistor. *Nat. Nanotechnol*. **7**, 174-179 (2012).
44. V. Vogel, M. Sheetz, Local force and geometry sensing regulate cell functions. *Nat. Rev. Mol. Cell Biol.* **7**, 265-275 (2006).
45. R. Parameswaran, K. Koehler, Y. Rotenberg Menahem, J. Burke Michael, J. Kim, K.-Y. Jeong, B. Hissa, D. Paul Michael, K. Moreno, N. Sarma, T. Hayes, E. Sudzilovsky, H.-G.

Park, B. Tian, Optical stimulation of cardiac cells with a polymer-supported silicon nanowire matrix. *Proc. Natl. Acad. Sci.* **116**, 413-421 (2019).

46. N. Ballan, N. Shaheen, G. M. Keller, L. Gepstein, Single-cell mechanical analysis of human pluripotent stem cell-derived cardiomyocytes for drug testing and pathophysiological studies. *Stem Cell Rep.* **15**, 587-596 (2020).
47. G. Q. Zhang, H. Wei, J. Lu, P. Wong, W. Shim, Identification and characterization of calcium sparks in cardiomyocytes derived from human induced pluripotent stem cells. *PLoS One* **8**, e55266 (2013).
48. S. Björk, E. A. Ojala, T. Nordström, A. Ahola, M. Liljeström, J. Hyttinen, E. Kankuri, E. Mervaala, Evaluation of Optogenetic Electrophysiology Tools in Human Stem Cell-Derived Cardiomyocytes. *Front. Physiol.* **8**, 884 (2017).
49. G. P. Farman, K. Tachampa, R. Mateja, O. Cazorla, A. Lacampagne, P. P. de Tombe, Blebbistatin: use as inhibitor of muscle contraction. *Pflugers Arch.* **455**, 995-1005 (2008).
50. B. P. Bean, C. J. Cohen, R. W. Tsien, Lidocain block of cardiac sodium channels. *J. Gen. Physiol.* **81**, 613-642 (1983).
51. H.-A. Lee, S.-A. Hyun, S.-G. Park, K.-S. Kim, S. J. Kim, Comparison of electrophysiological effects of calcium channel blockers on cardiac repolarization. *Korean J. Physiol. Pharmacol.* **20**, 119-127 (2016).
52. S. He, Y. Su, B. Ji, H. Gao, Some basic questions on mechanosensing in cell-substrate interaction. *J. Mech. Phys. Solids* **70**, 116-135 (2014).
53. M. L. Rodriguez, B. T. Graham, L. M. Pabon, S. J. Han, C. E. Murry, N. J. Sniadecki, Measuring the contractile forces of human induced pluripotent stem cell-derived cardiomyocytes with arrays of microposts. *J. Biomech. Eng.* **136**, 051005 (2014).
54. E. Karbassi, A. Fenix, S. Marchiano, N. Muraoka, K. Nakamura, X. Yang, C. E. Murry, Cardiomyocyte maturation: advances in knowledge and implications for regenerative medicine. *Nat. Rev. Cardiol.* **17**, 341-359 (2020)
55. A. Chen, E. Lee, R. Tu, K. Santiago, A. Grosberg, C. Fowlkes, M. Khine, Integrated platform for functional monitoring of biomimetic heart sheets derived from human pluripotent stem cells. *Biomater.* **35**, 675-683 (2014).
56. C. Bardy, M. van den Hurk, B. Kakaradov, J. A. Erwin, B. N. Jaeger, R. V. Hernandez, T. Eames, A. A. Paucar, M. Gorris, C. Marchand, R. Jappelli, J. Barron, A. K. Bryant, M. Kellogg, R. S. Lasken, B. P. F. Rutten, H. W. M. Steinbusch, G. W. Yeo, F. H. Gage, Predicting the functional states of human iPSC-derived neurons with single-cell RNA-seq and electrophysiology. *Mol. Psychiatry* **21**, 1573-1588 (2016).
57. T. Kraft, J. Montag, A. Radocaj, B. Brenner, Hypertrophic cardiomyopathy: cell-to-cell imbalance in gene expression and contraction force as trigger for disease phenotype development. *Circ. Res*. **119**, 992-995, (2016).
58. X. Lian, J. Zhang, S. M. Azarin, K. Zhu, L. B. Hazeltine, X. Bao, C. Hsiao, T. J. Kamp, S. P. Palecek, Directed cardiomyocyte differentiation from human pluripotent stem cells by modulating Wnt/β-catenin signaling under fully defined conditions. *Nat. Protoc.* **8**, 162-175 (2013).
59. R. Liu, J. Lee, Y. Tchoe, D. Pre, A. M. Bourhis, A. D'Antonio-Chronowska, G. Robin, S. H. Lee, Y. G. Ro, R. Vatsyayan, K. J. Tonsfeldt, L. A. Hossain, M. L. Phipps, J. Yoo, J. Nogan, J. S. Martinez, K. A. Frazer, A. G. Bang, S. A. Dayeh, Ultra-sharp nanowire

arrays natively permeate, record, and stimulate intracellular activity in neuronal and cardiac networks. *Adv. Funct. Mater.* **32**, 2108378 (2022).

60. Z. Fan, J. C. Ho, Z. A. Jacobson, R. Yerushalmi, R. L. Alley, H. Razavi, A. Javey, Wafer-scale assembly of highly ordered semiconductor nanowire arrays by contact printing. *Nano Lett.* **8**, 20-25 (2008).
61. Z. Wang, A. A. Volinsky, N. D. Gallant, Crosslinking effect on polydimethylsiloxane elastic modulus measured by custom-built compression instrument. *J. Appl. Polym. Sci.* **131**, 41050 (2014).
62. Q. Zhao, X. Wang, S. Wang, Z. Song, J. Wang, J. Ma, Cardiotoxicity evaluation using human embryonic stem cells and induced pluripotent stem cell-derived cardiomyocytes. *Stem Cell Res. Ther.* **8**, 54 (2017).
63. M. R. Salick, B. N. Napiwocki, J. Sha, G. T. Knight, S. A. Chindhy, T. J. Kamp, R. S. Ashton, W. C. Crone, Micropattern width dependent sarcomere development in human ESC-derived cardiomyocytes. *Biomaterials* **35**, 4454-4464 (2014).
64. W. Zhang, C. W. Kong, M. H. Tong, W. H. Chooi, N. Huang, R. A. Li, B. P. Chan, Maturation of human embryonic stem cell-derived cardiomyocytes (hESC-CMs) in 3D collagen matrix: Effects of niche cell supplementation and mechanical stimulation. *Acta Biomater.* **49**, 204-217 (2017).
65. C. Follmer, T. Colatsky, Block of delayed rectifier potassium current, IK, by flecainide and E-4031 in cat ventricular myocytes. *Circulation* **82**, 289-293 (1990).
66. M. Nelson Celeste, P. Jean Ronald, L. Tan John, F. Liu Wendy, J. Sniadecki Nathan, A. Spector Alexander, S. Chen Christopher, Emergent patterns of growth controlled by multicellular form and mechanics. *Proc. Natl. Acad. Sci.* **102**, 11594-11599 (2005).
67. N. Weber, K. Schwanke, S. Greten, M. Wendland, B. Iorga, M. Fischer, C. Geers-Knörr, J. Hegermann, C. Wrede, J. Fiedler, H. Kempf, A. Franke, B. Piep, A. Pfanne, T. Thum, U. Martin, B. Brenner, R. Zweigerdt, T. Kraft, Stiff matrix induces switch to pure β-cardiac myosin heavy chain expression in human ESC-derived cardiomyocytes. *Basic Res. Cardiol.* **111**, 1-16 (2016).
68. J. S. Ribeiro Alexandre, Y.-S. Ang, J.-D. Fu, N. Rivas Renee, M. A. Mohamed Tamer, C. Higgs Gadryn, D. Srivastava, L. Pruitt Beth, Contractility of single cardiomyocytes differentiated from pluripotent stem cells depends on physiological shape and substrate stiffness. *Proc. Natl. Acad. Sci.* **112**, 12705-12710 (2015).
69. M. C. Ribeiro, R. H. Slaats, V. Schwach, J. M. Rivera-Arbelaez, L. G. J. Tertoolen, B. J. van Meer, R. Molenaar, C. L. Mummery, M. M. A. E. Claessens, R. Passier, A cardiomyocyte show of force: A fluorescent alpha-actinin reporter line sheds light on human cardiomyocyte contractility versus substrate stiffness. *J. Mol. Cell. Cardiol.* **141**, 54-64 (2020).
70. G. Farnebäck, in *Image Analysis,* J. Bigun, T. Gustavsson, Eds. (Springer Berlin Heidelberg, Berlin, Heidelberg, 2003), pp. 363-370.

Acknowledgements:

Funding: J.Y. acknowledges support from the National Science Foundation (NSF) through CAREER CBET-1844904 and the generous material support from Prof. Charles Lieber at Harvard University. J.Y. also acknowledges supports from NSF ECCS-1917630, NSF DMR-2027102 and Army Research Office (W911NF2210027). Y.S. acknowledges support from NSF

CMMI-1846866. J.L acknowledges support from the National Institutes of Health (1R03EB028922-01). X.L acknowledges support from a Link Foundation Energy Fellowship. Part of the device fabrication work was conducted in the clean room of the Center for Hierarchical Manufacturing (CHM), an NSF Nanoscale Science and Engineering Center (NSEC) located at the University of Massachusetts Amherst.

Author contributions: J.Y. and H.G. conceived the project. H.G. performed experiments in device fabrication, characterizations, cell culture, imaging, and *in vitro* electrical recordings. F.Y. and Y.S. contributed cell supply and helped in cell culture. K.S. and J.L. performed mechanical simulations. X.D. performed image analysis. T.F. and S.F. designed the home-built current amplifier system for signal acquisition. X.L. assisted in device fabrication. J.Y. and H.G. wrote the paper. All authors discussed the results and implications and commented on the manuscript. **Competing interests**: The authors declare that they have no competing interests. **Data and materials availability**: All data needed to evaluate the conclusions in the paper are present in the paper and/or the Supplementary Materials.

Figure Legends

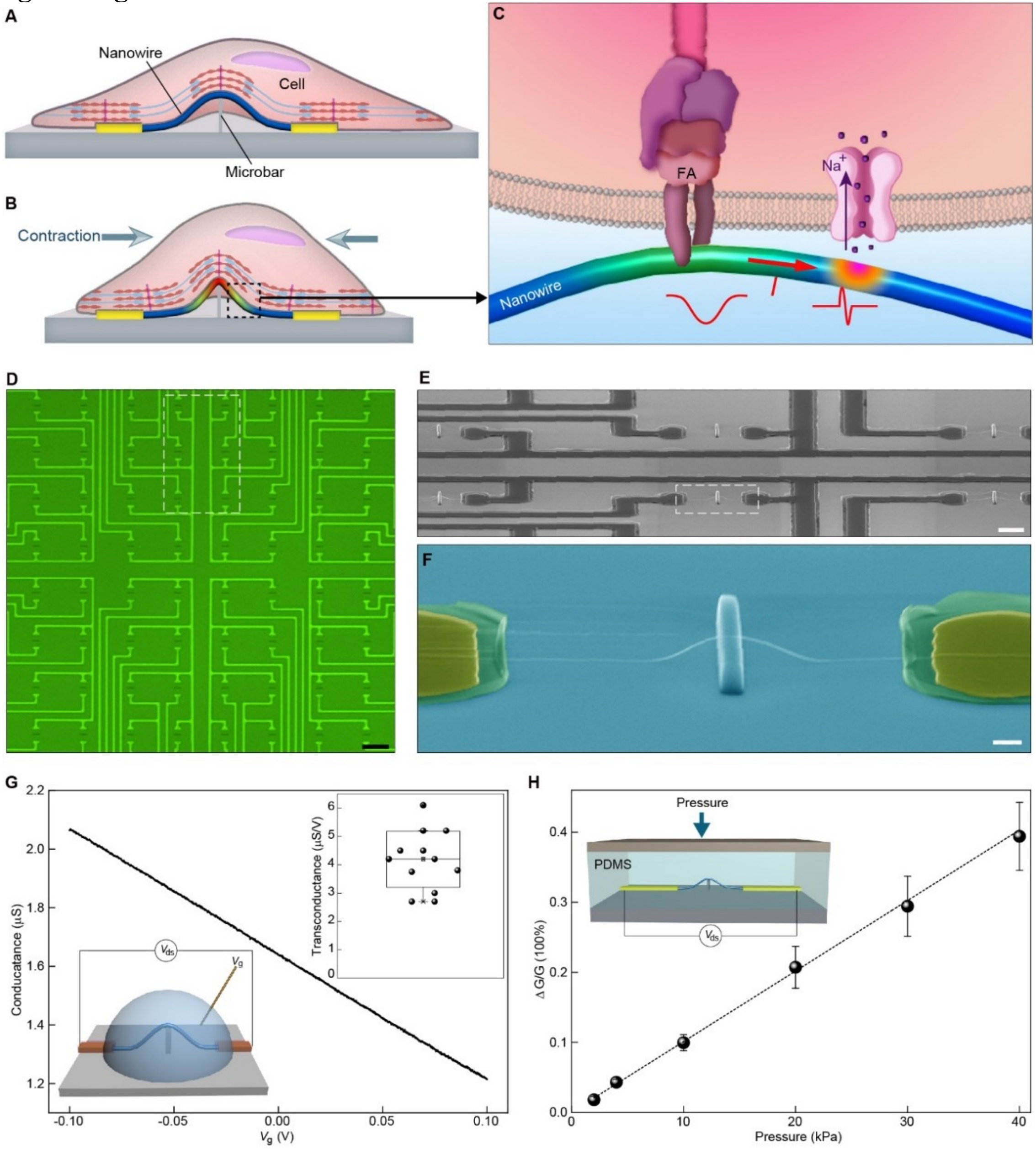

Fig. 1. Sensor concept and fabrication. (**A**) Schematic of the sensor structure and cell-sensor interface. (**B**) Schematic of the cell-sensor coupling during a contractile process. (**C**) Schematic of the electrical coupling and mechanical coupling (*e.g.*, through integrins of focal adhesion (FA)) between the nanowire and cell for the simultaneous detection of cellular force and AP. (**D**) Optical image of fabricated 8 × 8 sensors. Scale bar, 50 μm. (**E**) Scanning electron microscope (SEM) image of a 2 × 3 array corresponding to devices in the dashed box in (D). Scale bar, 10 μm. (**F**) (False colored) SEM image of a device corresponding to the one in the dashed box in (E). Scale bar, 1 μm. (**G**) Representative conductance change in a nanotransistor with respect to an applied water gate V_g (bottom schematic). The top inset shows the distribution of sensitivities in nanotransistors (N=12), with the average value of 4.2 ± 1.0 μS/V. (**H**) Average relative conductance change $\Delta G/G$ in nanotransistors (N=6) embedded in a polydimethylsiloxane layer (inset) with respect to applied pressure. More details can be found in fig. S4.

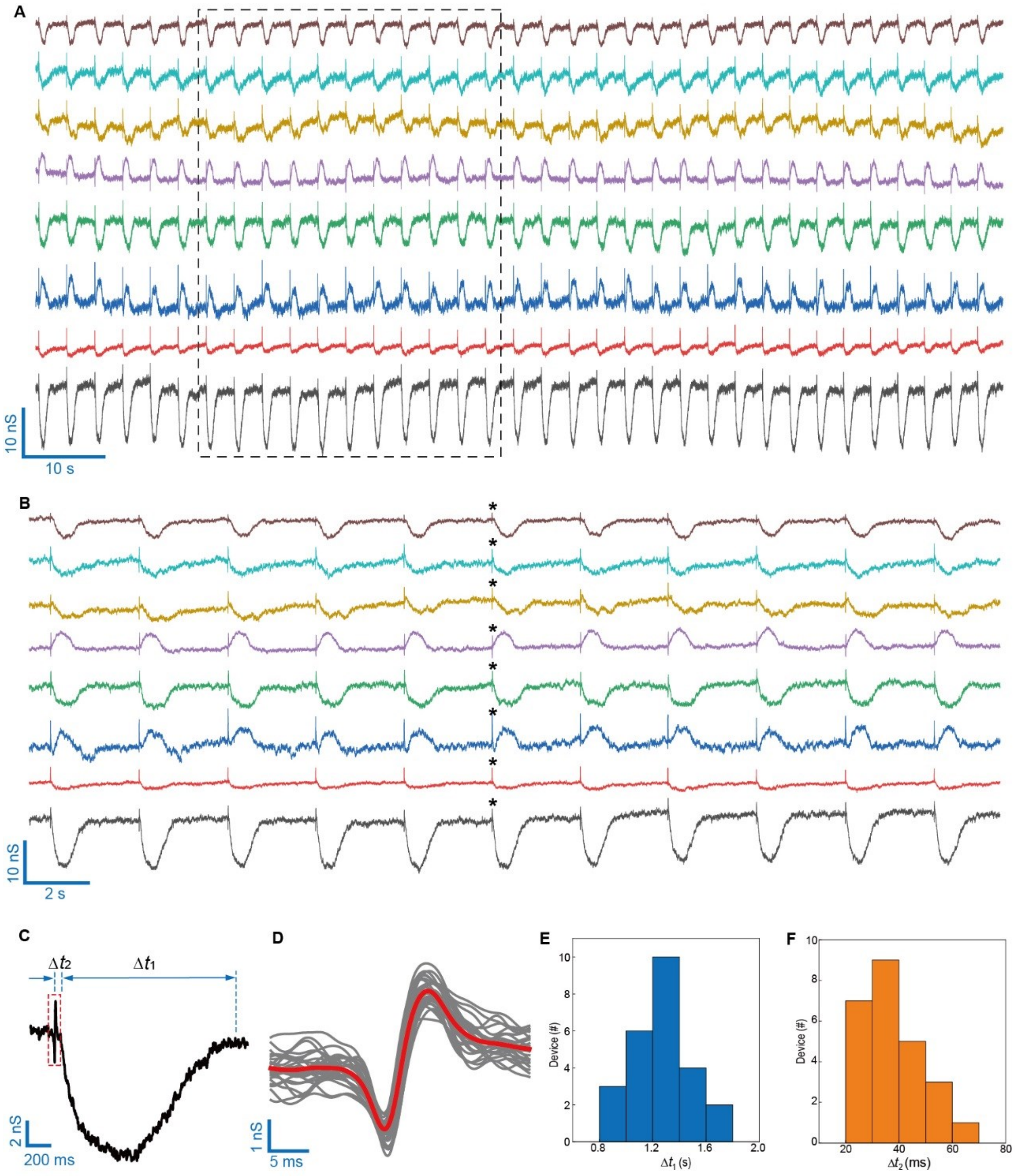

Fig. 2. Multiplexed recordings of AP and mechanical signals. (**A**) 8-channel recordings from cultured cardiomyocytes. (**B**) Zoomed-in signals from the dashed box in (a). The stars indicate the positions of narrow spikes corresponding to AP. (**C**) Zoomed-in signal in one period. Δt_1 is the width of the mechanical signal and Δt_2 the time delay between AP and the initiation of the mechanical signal. (**D**) Superimposed AP signals. The red line represents the mean waveform. (**E**) Histogram of Δt_1 ($N = 25$). (**F**) Histogram of Δt_2 ($N = 25$).

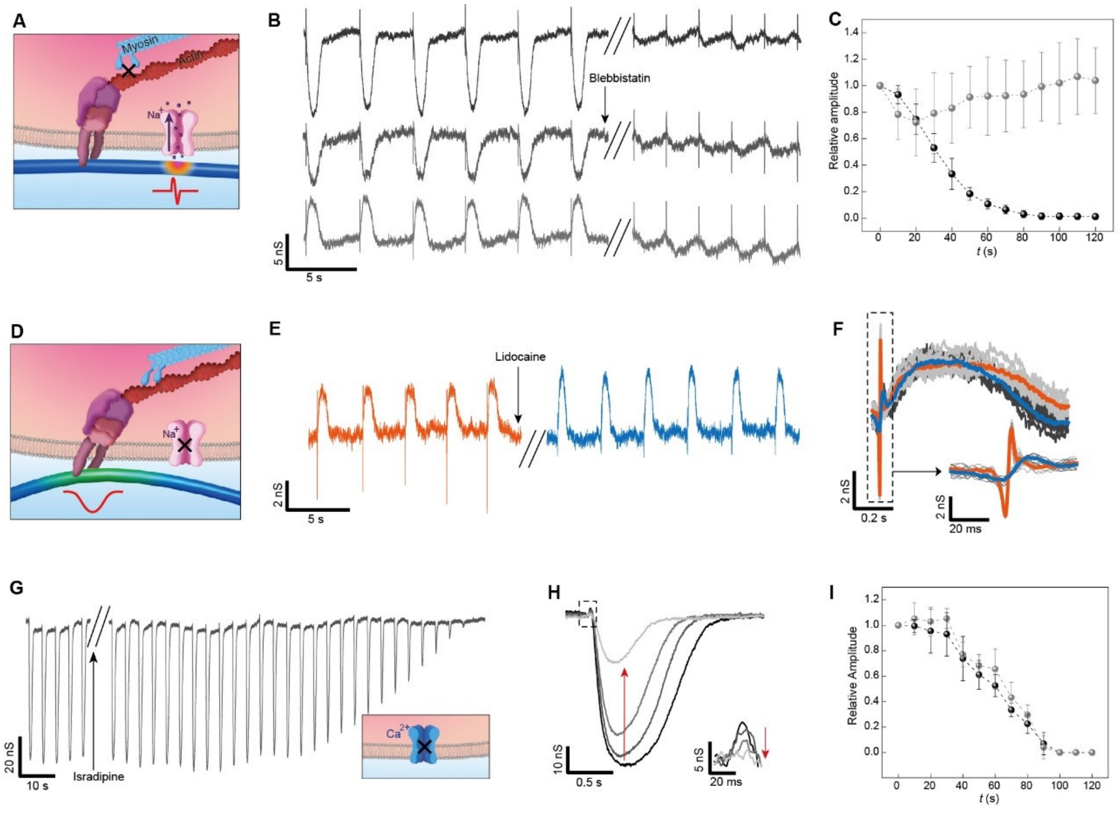

Fig. 3. Sensor implementation in detecting drug effects. (**A**) Schematic of blebbistatin effect on inhibiting cell contraction. (**B**) Electrical recordings from cardiomyocytes before (left) and after (right) adding blebbistatin. (**C**) Evolution in amplitude of the mechanical signals (black) and AP (gray) after adding blebbistatin. (**D**) Schematic of lidocaine effect on blocking Na^+ channels. (**E**) Recorded electrical signals before (orange) and after (blue) adding lidocaine. (**F**) Superimposed signals before (gray) and after (dark) adding lidocaine, with the orange and blue curves representing the corresponding mean waveforms. (**G**) Recorded electrical signals before (left) and after (right) adding isradipine, which blocks the Ca^{2+} channels (inset schematic). (**H**) Zoom-in signals in (G) over time (indicated by red arrows). The inset shows zoom-in AP in the dashed box. (**I**) Evolution in amplitude of the mechanical (black) and AP (gray) signals after adding isradipine.

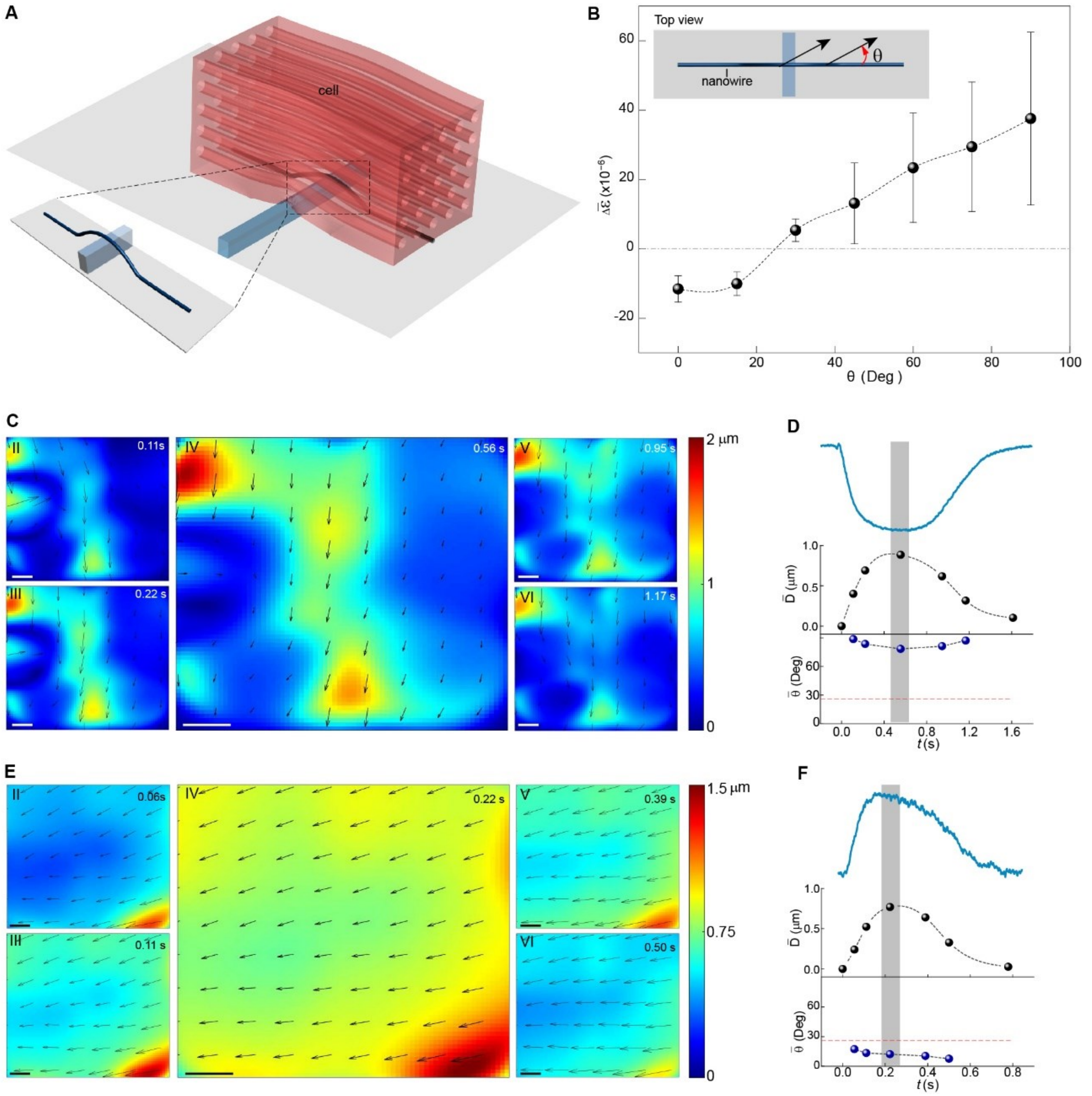

Fig. 4. Correlation between mechanical sensing signal and cellular motion. (**A**) Modeling of cell-sensor coupling. Details can be found in *Materials and Method*. (**B**) (Simulated) average net strain ($\overline{\Delta\varepsilon}$) induced in the nanowire with respect to θ, which characterizes the cell contractile direction with respect to the nanowire axis (inset). Due to structural symmetry, $0° \leq \theta \leq 90°$. $\overline{\Delta\varepsilon}$ was averaged across a typical contractile ratio range of 5-15% (fig. S22A). Simulation details are shown in fig. S18. (**C**) Evolution of local amplitudes (color) and vectors (arrows) of cellular motion at the device region during a contractile cycle (area ~35 × 35 μm^2). Scale bars, 5 μm. (**D**) Correlation between the electrical sensing signal (top), average amplitude ($\overline{D}$) (middle) and average angle $\overline{\theta}$ (bottom) of cellular motion at the sensor region. The data sets ($\overline{D}$, $\overline{\theta}$) correspond to frames in (C), with the 4th set (highlighted by gray bar) corresponding to frame IV. Note that the $\overline{\theta}$ value is insignificant at resting states (frames I and VII) and hence not plotted. The red dashed line indicates the simulated threshold angle of 25º. (**E**) Local amplitudes (color) and vectors (arrows) of cellular motion at another device region. Scale bars, 5 μm. (**F**) Corresponding electrical sensing signal (top), $\overline{D}$ (middle) and $\overline{\theta}$ (bottom) in (E).